

Article

Investigation of Non-Isothermal Kinetics and Thermodynamic Parameters for the Pyrolysis of Different Date Palm Parts

Emmanuel Galiwango ^{1,*}, Ali H. Al-Marzuoqi ^{1,*}, Abbas A. Khaleel ² and Mahdi M. Abu-Omar ³

¹ Department of Chemical and Petroleum Engineering, United Arab Emirates University, P.O. BOX 15551, Al Ain, UAE

² Department of Chemistry, United Arab Emirates University, P.O. BOX 15551, Al Ain, UAE; abbask@uaeu.ac.ae

³ Department of Chemistry and Biochemistry and Biochemistry, UC Santa Barbara Santa Barbara, Santa Barbara, CA 93106, USA; mabuomar@ucsb.edu

* Correspondence: emmag@uaeu.ac.ae (E.G.); hassana@uaeu.ac.ae (A.H.A.-M.); Tel.: +971-3713-6407 (E.G.); +971-3713-4470 (A.H.A.-M.)

Received: 26 October 2020; Accepted: 9 December 2020; Published: 11 December 2020



Abstract: Using the thermalgravimetric technique, we investigated the non-isothermal combustion kinetics of abundant and low-cost date palm wastes (leaflet, rachis, fibers, and their composite) as potential biomass energy sources. The kinetic and thermodynamic parameters were determined by Flynn–Wall–Ozawa (FWO), Kissinger–Akahila–Sunose (KAS), and Starink methods. Thermogravimetric analysis results showed a major peak for the degradation of volatiles between 127–138 °C with average percentage mass loss of 68.04 ± 1.5 , 65.57 ± 0.6 , 62.97 ± 5.5 , and 59.26 ± 3.2 , for rachis, composite, leaflet, and fibers, respectively. The FWO model showed the lowest activation energy, E_{α} , of 157 ± 25.6 , 158 ± 25.7 , 164 ± 40.1 , and 169 ± 51.8 kJ mol⁻¹ for the composite, rachis, leaflet, and fibers, respectively. The positive enthalpy values confirmed an endothermic pyrolysis reaction. For all models, a minimal difference of 4.40, 5.57, 6.55, and 7.51 kJ mol⁻¹ between activation energy and enthalpy for rachis, fibers, composite, and leaflet ensued, respectively. The KAS model was best suited to describe chemical equilibrium with average ΔG values of 90.3 ± 28.8 , 99.3 ± 34.9 , 178.9 ± 27.3 , and 186.5 ± 38.2 kJ mol⁻¹ for rachis, fibers, composite, and leaflet, respectively. The reaction mechanism by the Malek and Popescu methods was $(g(\alpha) = [-\ln(1 - \alpha)]^{\frac{1}{4}})$ across the conversion range of 0.1–0.9 for all heating rates. The high energy content and volatile matter combined with low energy barriers make date palm waste a potential candidate in a biorefinery.

Keywords: lignocellulosic biomass; waste-to-energy; reaction mechanism; date palm waste; Malek and Popescu methods

1. Introduction

Sunlight, by far, is the most abundant carbon-neutral source of energy. Insolation releases 4.3×10^{20} J every hour, enormous energy more than the total energy requirement on Earth yearly [1]. The global energy consumption has risen from 13 TW in 2015 [1] to 18 TW in 2019 [2]. The increasing population, technology advancement, and economic growth will raise energy demand to about 30 TW by 2050 and 46 TW by the end of the century [1,3]. The current most dependable source of energy is fossil fuels [4]; however, even with robust energy conservation and efficient measures, the non-renewable nature of fossil fuels is not sustainable because it is finite. Furthermore, the incessant combustion of fossil fuels to provide energy has some negative environmental impacts such as anthropogenic

global warming, attributed to the emissions of greenhouse gases (GHGs). Among the GHG major contributors is CO₂ whose atmospheric concentrations has risen by 1.3% to 33 Gigatons in 2018 [2]. In addition, NO_x emissions are projected to increase due to the increase in coal-fired energy generating operations. China currently depends on coal to meet about 70% of its energy requirements and coal usage is projected to increase [5]. Coal processing used to generate energy pollutes the environment with NO_x emissions. Emission reduction technologies such as CO₂ capture and storage, selective and non-selective catalytic systems have yielded less in terms of controlling global emissions largely due to technology cost and deficiency in emission control commitment by stake holders [6]. In an attempt to reduce the industrial emissions, several cleaner production technologies and good practices such as re-engineering approaches, substituting toxic for less toxic and renewable inputs have been recommended [7,8]. Alternatively, sustainable and renewable fuels (such as lignocellulose biomass) can reduce toxic industrial emissions and meet the future global energy demands because they have competitive energy capacity and low cost advantage [9,10]. Moreover, the policy implications of implementing renewable biomass is high motivation for their development. Some policy implications including competition between food, feed, and fuels can be greatly reduced if the increase in the production of biomass for energy is balanced by agricultural management improvements and reliance on perennial lignocellulosic biomass in degraded and marginal areas. In addition, major environmental concerns such as biodiversity, quality of the soil and availability of water, need attention. This can be achieved by choosing appropriate bioenergy systems and implementing enough land use planning. Choosing suited biomass sources (such as using residual biomass like date palm waste and perennial crops) can secure positive greenhouse gas (GHG) balances of bioenergy systems, while preventing direct and indirect land use changes that cause high greenhouse gas emissions [11]. In the context of emissions reduction, biomass co-firing can produce power output to 10% of coal plant and thus, reduce CO₂ and NO_x emissions by 10% or even higher [6,12]. In order to reduce the negative effects such as price volatility and future availability arising from fossil-based feedstocks in chemical and manufacturing industry, biorefineries are projected to be among the future chemical and energy drivers [13]. The biorefinery concept relies on different renewable biomasses such as algal, lignocellulose, and plant biomass. The varying and wide processing range of processing technologies and the physical, and chemical properties of different biomasses remains a challenge to the fast development of biorefinery technology [14]. In addition, there are challenges surrounding the design and optimal development of biorefinery against market uncertainties [13]. Designing an optimal biorefinery against market uncertainties has been reported, highlighting the advantages of lignocellulose over other biomasses like algal biomass [13,15]. In addition, the economic risk and technical and conceptual approaches have been quantitatively studied and factors such as choice of biomass raw material and robust processing technology remain important for the development of an optimal biorefinery [14,15]. However, the existing operational biorefinery process technologies largely depend on copied processes from oil refineries and this has some limitation on biorefinery competitiveness, actual long-term environmental impact assessment, reduced profitability, and challenges to process some lignocellulose biomass [14,16]. Thus, more research on different biorefinery feedstocks and processing approaches is needed to bridge the uncertainties around the variance in physico-chemical properties and insufficient knowledge on robust processing technologies of lignocellulose biomass. The fundamental questions that have not been addressed are the utilization of different parts of the same waste to assess their differences in terms of physical and chemical properties and their suitability to be configured in a biorefinery model. Furthermore, studies of pyrolysis kinetic and thermodynamic parameters to predict the reaction mechanism are still insufficient. This research aims to characterize a new biorefinery candidate using simple and robust thermogravimetric analysis data to determine the pyrolysis kinetics and thermodynamic properties of date palm lignocellulose waste biomass. The research outcomes will also lead to the prediction of the reaction mechanism taking place during the pyrolysis involving pseudo-chemical components such as hemicellulose, cellulose, and lignin.

Lignocellulose biomass stores some of the solar energy in its tissues through photosynthesis and this process guarantees carbon sequestration for a prolonged period [17]. The energy density of liquid fuels from plants (47 MJ kg^{-1}) is more than one magnitude higher than common rechargeable Li-ion batteries (0.8 MJ kg^{-1}) [18]. Lignocellulose biomass is regarded as a viable source for sustainable energy due to its high energy density and wide global spread [18]. Researchers have reported on its prospects to produce biomass-based energy on both small- and large-scales [19–22]. However, the differences in the origin and period of growth can result in varying physicochemical properties of biomass [23]. Therefore, the cost of production is key to processing different biomass-based energy. Like conventional energy crops (such as grasses), wood-based biomass waste requires no fertilizers during growth and has no competition with nutritional or industrial consumptions, thus offsetting any production cost. In addition, policies such as renewable fuel standards in the USA and the European rules on renewable energy development favor bioenergy development, which will significantly reduce the cost of biofuel production [24]. Different technologies such as direct combustion, fermentation, and pyrolysis are used to exploit the energy resource stored in lignocellulose-based biomass. Among these technologies, pyrolysis can convert biomass into three forms of biofuel: bio-oil, gas, and biochar [25–29].

Biomass pyrolysis involves complex and simultaneous reactions [30,31], attributed to the differences in biomass type and pyrolysis conditions [32,33]. Understanding the pyrolytic response of certain biomass is vital to optimizing its thermal conversion to desirable products. Such thermal responses (conversion pathways and reaction mechanisms) are dependent on the kinetic and thermodynamic profiles of the process [32]. General kinetic models on different lignocellulosic biomass have been suggested [34,35]. However, developing accurate kinetic models to account for all sub-reactions taking place, remains a challenge [36]. However, thermogravimetric analysis (TGA) can provide a deeper understanding of the kinetics and reaction mechanisms of a pyrolysis process [37–39]. Using TGA data and different models to predict pyrolysis and kinetics properties of coal and other biomasses like algae, lignocellulose, etc. have often been used. The single reaction model (SRM) is the simplest among all models and this focuses on first order reactions. SRM is valid over a narrow range of temperatures, hence its limited applicability [40]. Hence, other models like the distributed activation energy model (DAEM) and model-free methods are famously used. The DAEM model has practically been used for a single distribution of activation energy. However, due to multistage reactions involved during pyrolysis, single activation energy distribution cannot be guaranteed [41]. Therefore, the model-free methods such as FWO, KAS, and Starink models have received attention. The models have advantages such as the ease for the determinations of kinetic parameters and can cover a wide range of activation energy over a wide range of temperatures without knowledge about the reaction model [42]. In addition, model free methods can be used to calculate the activation energy at varying heating rates at the same conversion value [43]. Despite the promising growing applicability of the model free methods, a lot has been studied on coal solid fuels. Therefore, some assumptions made during coal processing may not be valid for other feedstocks such as lignocellulose biomasses. In addition, some model-free methods like KAS does not depend on isoconversion to calculate the activation energy, but rather assumes a constant activation energy [43]. This means one model-free method alone cannot be used to predict the reaction kinetics of biomass. However, the wide application of the model free methods to mainly coal provides more opportunity for research on solid state kinetic studies in many other renewable biomasses whose kinetic, thermodynamic, and physico-chemical characteristics are known to vary depending on biomass type, period of growth, etc.

Recently, the pyrolysis of date palm waste was conducted extensively [44–46]. However, hardly any reports on the non-isothermal kinetics and thermodynamics have been reported using the date palm waste parts (DPWP). Therefore, this research utilized low-cost and locally abundant DPWP to model non-isothermal pyrolysis kinetics. Furthermore, we proposed the application of free-model methods to determine the kinetics, plausible reaction mechanism, and thermodynamic parameters for the pyrolysis of these wastes.

The DPWP considered in this research came from over 40 million date palm trees in the UAE, which generate about 500,000 tons of non-edible waste annually [47]. Furthermore, waste from the edible fruit of the date palm is also generated. For instance, at the UAE University farm (where raw materials for this research were sourced), for every 1 kg of date fruits produced, 400 g of seed waste is generated. However, we did not cover this type of waste due to the nutritional health values probably attributed to such wastes. Currently, all the waste is used for low energy values such as art and craft, and or burned, thus polluting the environment. This study is vital to understanding the kinetics, thermodynamics, and reaction mechanism of pyrolyzing date palm waste. In the future, it could be considered for biorefinery generation of bioenergy.

2. Materials and Methods

2.1. Sample Preparation and Determination of Physicochemical Properties

The DPWP (i.e., leaflet (L), rachis (R), fiber (F), and composite (M)) were collected from UAE University Farm, Al Foah, in the UAE in June 2019, released from mature date palm trees (>10 years old). The M sample was a bulk ratio of 0.5:2:0.6 for L, R, and F, respectively. The samples were ground and sieved to a particle size of 180 μm to aid effective heat transfer during pyrolysis. Then, aliquots of the samples were analyzed using standard protocols to determine the moisture content (ASTM E1755-01, 2007), ash content (ASTM E872-82, 2006), volatile matter (ASTM E871-82, 2006), fixed carbon (ASTM D3172-07a), and high heating value (HHV) [48]. Experiments were performed in triplicate. The ultimate analysis was determined by an automatic elemental analyzer (Flash EA1112, CE Instruments). The inorganic elemental analysis was conducted on an inductively-coupled plasma optical emission spectrometer (Varian 710-ES, USA) [49]. In brief, DPWP samples (5 g each) were pre-homogenized with nitric acid (5 mL, 65%), hydrofluoric acid (2 mL, 40%), and DI water (8 mL), followed by ultrasonication for 8 h at 90 °C (ANALAB steel ultrasonic bath, India). The pre-homogenization stage helps in effective digestion with nitric acid where organic matter is oxidized to CO_2 and NO , resulting in the formation of soluble nitrates with most elements that can then be analyzed. The samples in the Nalgene vessel, placed in a 100 °C water bath, were kept under constant stirring for 4 h until a homogeneous paste was obtained. The pre-homogenized DPWP (0.4 g) was digested with nitric acid (4 mL, 65%) before being diluted to working concentrations before analysis.

2.2. Lignin and Carbohydrate Analysis

The extractive-free DPWP samples were analyzed for lignin and carbohydrate contents using standard NREEL methods [50]. The extractives in DPWP were determined gravimetrically after Soxhlet extraction (48 h) with ethanol and benzene (1:2, *v:v*) [51]. In detail, the soluble and insoluble parts of the lignin were determined by digesting aliquots of L, R, F, and M ($1.0 \pm 0.1\text{g}$) each with sulfuric acid (4 mL, 72%) at 37 °C for 1 h. Further dilution with deionized water (DI) to achieve secondary hydrolysis (3% sulfuric acid) was carried out in an autoclave at 121 °C for 1 h [50]. After filtration, the insoluble lignin was obtained gravimetrically, whereas the liquid aliquot was used to obtain the acid-soluble lignin and the carbohydrate. Using a Shimadzu UV-1800 UV spectrophotometer, the acid-soluble lignin was determined at 205 nm and absorptivity value ($110 \text{Lg}^{-1} \text{cm}^{-1}$), following the TAPPI method UM-250 [51,52]. Furthermore, the solubilized carbohydrate aliquot (1 mL) was diluted with DI water to the mark of the volumetric flask (10 mL), followed by filtration using a 13 mm diameter syringe filter with a 0.2 μm pore size PTFE membrane. Soluble carbohydrates were quantified using HPLC (two Hi-plex columns, 7.7 mm \times 300 mm, Agilent Technologies 1260 Infinity, Santa Clara, CA, USA).

2.3. Thermogravimetric Analysis (TGA)

The pyrolytic properties of the DPWP sample were investigated using thermogravimetric analysis, TGA (Q500 series, TA Instruments, New Castle, DE, USA). First, 6 ± 1.0 mg of each DPWP was equilibrated at 25 °C for 5 min before heating to 900 °C at heating rates of 10, 15, 20, and 25 °C/min

under a N₂ flow of 20 mL/min. While thermal decomposition proceeded to completion, the change in weight was continuously recorded as a function of temperature and time.

2.4. Scanning Electron Microscopy (SEM)

The structural morphologies of the L, R, F, and M samples were observed using a JEOL Neoscope JCM-5000, Tokyo Japan microscope following the method in the literature [53]. Before the scanning electron microscope (SEM) examination, the samples were gold (Au/C)-coated using a vacuum sputter fixed on the sample holder. The images were captured on a spot size of 40 using 10 kV.

2.5. Fourier-Transform Infrared (FTIR) Spectroscopy

To identify the possible differences in the functional groups on L, R, F, and M samples, Fourier transform infrared (FTIR) spectra were obtained with a Jasco FT/IR-4700, USA spectrometer. The analysis was performed analogous to the literature methods within the spectral range of 4000–400 cm⁻¹ wavelengths using 32 scans and 4 cm⁻¹ resolution to the background spectra recorded [54,55].

2.6. Non-Isothermal Kinetics and Thermodynamic Parameter Mathematical Modeling

Finally, the TGA data were further analyzed to calculate the non-isothermal kinetic and thermodynamic parameters using the model-free equations of Flynn–Wall–Ozawa (FWO), Kissinger–Akahira–Sunose (KAS), and Starink [56]. These model-free methods were chosen because no previous knowledge of reaction mechanisms is required to determine the reaction kinetic energy [57]. We also estimated the pre-exponential factor (A) and thermodynamic parameters (enthalpy (ΔH), entropy (ΔS), and Gibb's free energy (ΔG)) [37]. The pre-exponential factor is heavily linked with the kinetic equation and the activation energy. Therefore, to accurately determine A and to avoid the introduction of unknowns, the equation used must involve a kinetics model [58]. Thus, the choice of the FWO, KAS, and Starink model free methods for this research.

3. Results and Discussion

3.1. Date Palm Waste Parts (DPWP) Characteristics

The results of the proximate and ultimate analyses are shown in Table 1. The former gives details of sample chemical composition and the latter gives the quantitative results of the organic elements present in the samples. The low moisture and ash contents were important in the reactor configuration. Additionally, the generally high volatile matter implies that all parts of DPWP were highly pyrolyzable into biobased products. However, the samples exhibited common high oxygen content, low carbon to hydrogen ratio, and no nitrogen and sulfur contents, which is characteristic of most lignocellulosic biomasses. The high oxygen content remains a challenge to the full conversion of biomass on a commercial scale. Furthermore, the proximate and ultimate analyses results were similar to those of other energy crops such as *Arundo donax* (volatile matter = 68.4%, C = 42.7, H = 7.5, O = 48.7) and *miscanthus giganteus* (volatile matter = 78.8%, C = 43.7, H = 5.7, O = 44.8) [59].

Table 1. Physicochemical analysis of date palm waste parts (DPWP) (dried basis).

| | DPWP Samples | | | |
|---------------------------------|--------------|--------------|--------------|---------------|
| | Leaflet (L) | Rachis (R) | Fibers (F) | Composite (M) |
| Proximate analysis | | | | |
| Moisture content (wt.%) | 7.30 ± 0.2 | 6.72 ± 0.4 | 6.44 ± 0.1 | 7.02 ± 0.2 |
| Volatile matter (wt.%) | 75.84 ± 0.01 | 78.62 ± 0.04 | 77.40 ± 0.01 | 76.64 ± 0.01 |
| Ash content (wt.%) | 12.71 ± 0.1 | 6.12 ± 0.1 | 8.24 ± 0.2 | 6.56 ± 0.4 |
| Fixed carbon (wt.%) | 7.12 ± 0.01 | 5.40 ± 0.01 | 9.02 ± 0.02 | 6.24 ± 0.01 |
| Ethanol/benzene extractives (%) | 29.00 ± 0.6 | 21.07 ± 0.4 | 9.12 ± 0.1 | 22.03 ± 0.6 |

Table 1. Cont.

| | DPWP Samples | | | |
|----------------------------|--------------|-------------|-------------|---------------|
| | Leaflet (L) | Rachis (R) | Fibers (F) | Composite (M) |
| Ultimate analysis | | | | |
| C (%) | 45.20 | 43.72 | 43.12 | 42.08 |
| H (%) | 6.00 | 5.80 | 5.81 | 5.62 |
| O (%) | 47.80 | 49.87 | 50.20 | 48.81 |
| HHV (MJ kg ⁻¹) | 17.96 | 17.28 | 17.01 | 16.53 |
| Insoluble lignin (wt.%) | 19.02 ± 0.1 | 16.03 ± 0.1 | 20.28 ± 0.4 | 18.20 ± 0.2 |
| Soluble lignin (wt.%) | 1 ± 0.01 | 1 ± 0.04 | 1 ± 0.02 | 1 ± 0.01 |
| Glucan (wt.%) | 21 ± 0.03 | 32 ± 0.01 | 33 ± 0.01 | 30 ± 0.02 |
| Xylan (wt.%) | 11 ± 0.01 | 19 ± 0.01 | 17 ± 0.01 | 16 ± 0.01 |
| Arabinan (wt.%) | 2 ± 0.02 | 3 ± 0.02 | 2 ± 0.01 | 3 ± 0.01 |
| Elemental Analysis (ppm) | | | | |
| K | 33.0 ± 0.6 | 28.9 ± 0.6 | 30.8 ± 0.0 | 26.3 ± 0.4 |
| P | 10.9 ± 0.2 | 16.7 ± 1.8 | 6.7 ± 1.6 | 12.0 ± 0.4 |
| Ca | 196.5 ± 8.0 | 158.2 ± 20 | 305.9 ± 28 | 166.6 ± 12 |
| Mg | 24.0 ± 2.2 | 21.4 ± 3.0 | 46.6 ± 8.0 | 21.2 ± 2.0 |
| Na | 8.7 ± 2.3 | 11.5 ± 1.4 | 26.5 ± 3.6 | 9.3 ± 1.6 |

3.2. Thermogravimetric Analysis (TGA)

Figure 1 shows the biomass isoconversion and differential thermograms (DTG) against the temperature of each DPWP. All samples showed similar thermal degradation trends at all heating rates. At ≤ 350 °C, the conversion curves increased slightly with temperature for all samples. However, at > 350 °C, the conversion curves changed in reverse order for all heating rates. The two distinct trends signify a likely difference in the degradation chemistry of components under combustion, below and after 350 °C. Below 350 °C can plausibly be associated with the thermal decomposition of extractives, hemicellulose, and part of the cellulose contained in the samples. However, above 350 °C, this higher degradation temperature is characteristic to the degradation of complex lignin. In addition, the similarity in the conversion trends at all the heating rates indicate that the heating rate does not influence the chemical transformation of the samples at specified temperature regions. Therefore, a lower heating rate could be used to maximize the thermal conversion of DPWP to bio-products in a biorefinery [31]. The DTG versus temperature curves showed similar trends among the samples. All samples exhibited thermal hysteresis (i.e., the decrease in mass with an increase in temperature), resulting in shorter reaction time. The observed thermal degradation patterns are prevalent in many types of lignocellulosic biomass [60,61].

Tables 2 and 3 show the temperature range and major stages of weight loss associated with the temperature regimes. The mass loss in Stage-I represents inherent moisture within both intra- and inter-cellular void spaces of the biomass, whereas Stage-II represents the region of the main thermal decomposition involving the release of volatile matter, mainly from hemicellulose, cellulose, and lignin [62]. The average mass loss followed the order $R > M > L > F$. In Stage-III, the pyrolysis of lignin, carbonaceous matter, and some char oxidation were observed [60,63]. The last stage represents the charring process and ash formation. Using DTG from TGA data, the chemical kinetics of the pyrolysis reaction can be predicted and described.

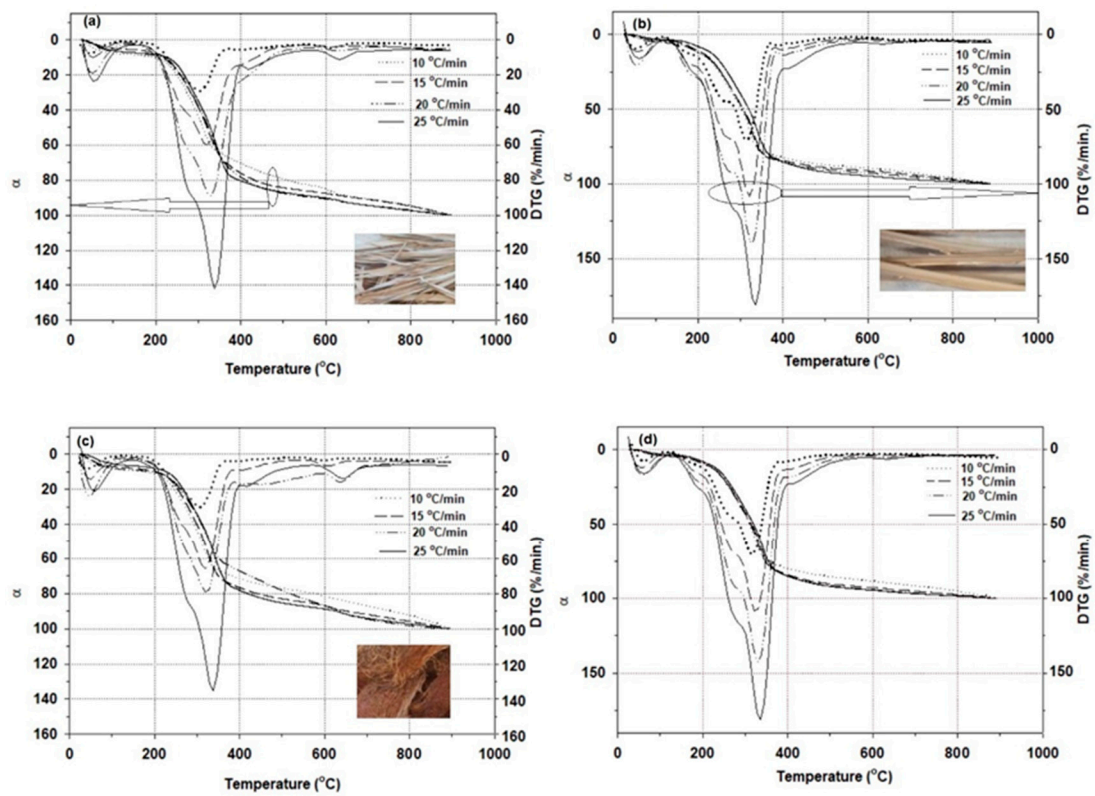


Figure 1. The TG and DTG of (a) leaflet (L), (b) rachis (R), (c) fibers (F), and (d) composite (M) at heating rates of 10, 15, 20, and 25 °C min⁻¹.

Table 2. Characteristic temperatures associated with mass loss during the pyrolysis of DPWP.

| Heating Rate (°C min ⁻¹) | Temperature (°C) | | | | | | | | | | | |
|---|------------------|----------------|----------------|----------------|----------------|------------------|------------------|----------------|----------------|----------------|----------------|------------------|
| | T _{min} | T ₁ | T ₂ | T ₃ | T ₄ | T _{max} | T _{min} | T ₁ | T ₂ | T ₃ | T ₄ | T _{max} |
| | Leaflet (L) | | | | | | Rachis (R) | | | | | |
| 10 | | 129 | 198 | 260 | 372 | | | 127 | 197 | 280 | 370 | |
| 15 | 30 | 133 | 200 | 269 | 385 | 900 | 30 | 128 | 203 | 286 | 383 | 900 |
| 20 | | 137 | 205 | 283 | 387 | | | 129 | 207 | 292 | 394 | |
| 25 | | 140 | 210 | 288 | 398 | | | 131 | 212 | 300 | 398 | |
| | Fibers (F) | | | | | | Composite (M) | | | | | |
| 10 | | 127 | 201 | 262 | 383 | | | 130 | 195 | 277 | 378 | |
| 15 | 30 | 129 | 209 | 269 | 389 | 900 | 30 | 132 | 196 | 288 | 389 | 900 |
| 20 | | 131 | 212 | 273 | 391 | | | 133 | 197 | 289 | 394 | |
| 25 | | 142 | 220 | 290 | 396 | | | 135 | 210 | 292 | 398 | |

Table 3. Mass loss during the Stages I–III of the DPWP decomposition.

| Stages | Temperature (°C) | Heating Rate (°Cmin ⁻¹) | | | |
|---------------------------------|----------------------------------|-------------------------------------|-------|-------|-------|
| | | 10 | 15 | 20 | 25 |
| Leaflet (L) | | | | | |
| Stage-I, WL% | T _{min} –T ₁ | 6.07 | 5.81 | 5.87 | 5.89 |
| Stage-II, WL% | T ₁ –T ₄ | 58.39 | 63.48 | 63.01 | 66.98 |
| Stage-III, WL% | T ₄ –T _{max} | 28.54 | 23.07 | 23.46 | 20.0 |
| Final residue at 900–100 °C (%) | | 7.0 | 7.64 | 7.66 | 7.13 |

Table 3. Cont.

| Stages | Temperature (°C) | Heating Rate (°Cmin ⁻¹) | | | |
|---------------------------------|----------------------------------|-------------------------------------|-------|-------|-------|
| | | 10 | 15 | 20 | 25 |
| Rachis (R) | | | | | |
| Stage-I, WL% | T _{min} -T ₁ | 5.92 | 6.32 | 6.54 | 5.80 |
| Stage-II, WL% | T ₁ -T ₄ | 66.22 | 67.54 | 68.89 | 69.49 |
| Stage-III, WL% | T ₄ -T _{max} | 20.52 | 18.59 | 14.09 | 14.61 |
| Final residue at 900–100 °C (%) | | 7.34 | 7.55 | 10.48 | 10.10 |
| Fibers (F) | | | | | |
| Stage-I, WL% | T _{min} -T ₁ | 6.63 | 5.96 | 6.96 | 5.89 |
| Stage-II, WL% | T ₁ -T ₄ | 54.86 | 60.74 | 58.92 | 62.53 |
| Stage-III, WL% | T ₄ -T _{max} | 25.91 | 25.16 | 25.05 | 23.58 |
| Final residue at 900–100 °C (%) | | 12.6 | 8.14 | 9.07 | 8.0 |
| Composite (M) | | | | | |
| Stage-I, WL% | T _{min} -T ₁ | 6.96 | 7.2 | 6.89 | 6.56 |
| Stage-II, WL% | T ₁ -T ₄ | 64.88 | 65.90 | 65.31 | 66.20 |
| Stage-III, WL% | T ₄ -T _{max} | 22.55 | 19.83 | 16.17 | 13.56 |
| Final residue at 900–100 °C (%) | | 5.61 | 7.07 | 11.63 | 13.68 |

3.3. Micrographic Image Properties

Each DPWP was evinced for its characteristic structural morphology, observed at ×1500 magnification. L showed a relatively regular cylindrical shape with irregular pore diameters (Figure 2A), whereas R exhibited irregular structures mixed with spiral ring-shaped morphologies (Figure 2B). Unlike L and R, the F sample had closed-end regular cylindrical rods with measurable external diameter, with an average outer diameter of 94.81 μm (Figure 2C). In Figure 2D, a clear representation of M with both regular and irregular morphologies was observed. Generally, the SEM results inform the co-pyrolysis synergy such as volatile matter release capabilities and the properties of the biochar formed [64]. However, because the quantity of biochar left after TGA analysis was too small to be used for replicate analysis, further SEM analysis was not performed.

3.4. FTIR Analysis of DPWP

Through the FTIR analysis of DPWP, we observed that all DPWP showed similar functional groups with varying spectral intensities across the measured spectrum (Figure 3). The absorption bands around 1260–1034 cm⁻¹ were assigned to C–O–C and C–O bond stretching in the aryl ether groups present in cellulose and lignin [40,41]. The spectral bands at 1649, 1527, and 1649 cm⁻¹ were attributed to the C=C vibration of the aromatic ring, C–H bending, and C=C aromatic skeletal vibrations, respectively [41,42]. Furthermore, the bands in the range between 2371 and 2098 cm⁻¹ were characteristic of C=O stretching present in the carboxylic, ketone, and aldehyde groups [42]. Whereas the spectral bands between 2925 and 2846 cm⁻¹ were assigned to the C–H stretching of the aldehyde and hydrocarbon groups [43]. Finally, the spectral in the region of 3900–3200 cm⁻¹ was due to O–H bond vibrations [42]. These FTIR results were like those reportedly found in other biomasses [42,43].

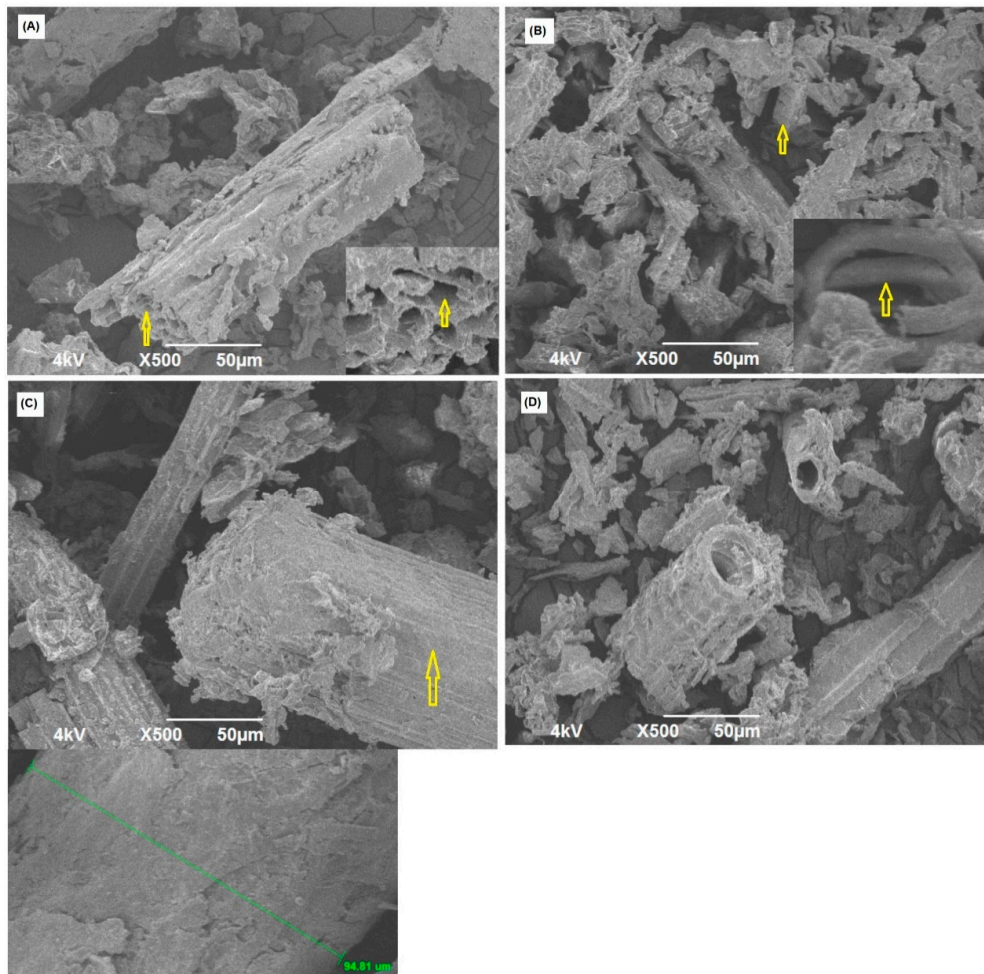


Figure 2. Scanning electron micrographs of DPWP: (A) leaflet (L), (B) rachis (R), (C) fibers (F), and (D) composite (M) at 500 \times magnification.

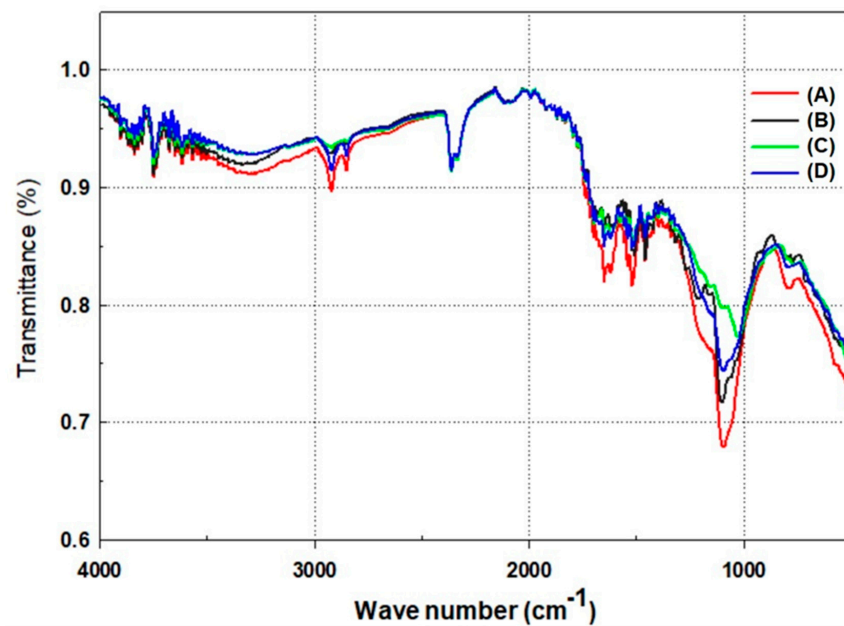


Figure 3. The Fourier transform infrared (FTIR) spectra of (A) leaflet (L), (B) rachis (R), (C) fibers (F), and (D) composite (M) samples.

3.5. Analyses of Kinetic and Thermodynamic Parameters

The activation energies of each DPWP were calculated using the three model-free techniques of FWO, KAS, and Starink. As illustrated in Figures S1–S3 (Supplementary Materials), the fitting of the experimental data with the kinetic models for all DPWP showed similar linear trends.

Pyrolysis of biomass involves complex heterogeneous reactions, whose chemical kinetics and reaction dynamics are influenced by many factors such as the activation energy (E_α) and pre-exponential factor [34]. Therefore, for each conversion, α , the activation energy (E_α) was determined from the corresponding slope of the model, while the pre-exponential factor (A) and thermodynamic parameters were calculated using relevant equations [37]. Table 4 shows the results of the average values of E_α , A , and thermodynamic parameters of L, R, F, and M. In addition, in a range of conversion (0.1–0.9), the values of E_α , A , and thermodynamic parameters are shown in Tables S1–S4. The correlation coefficient, R^2 (for the regression lines in Figures S1–S3 for the models) were above 0.98 for all samples. Therefore, the models described the data with 98% accuracy.

As shown in Table 4, the average activation energy values were lowest and highest in the composite and fiber samples, respectively. Furthermore, in Tables S1–S4, activation energies for all the samples increased exponentially with increasing isoconversion. The trend for the dependency of activation energy on conversion was linked to the pyrolysis of lignocellulose components in the samples [65]. Irrespective of the model, at lower conversions, the activation energy was low due to the thermal decomposition of hemicellulose and cellulose. Activation energy continued to rise at higher conversions due to the pyrolysis of the lignin complex structure [65]. The FWO model evinced a lower E_α compared to those of the KAS and Starink, whose activation energies were similar. Specifically, the M sample had the lowest activation energy values from the FWO model. However, the value obtained by KAS and Starink were slightly higher than those for the R sample. This was possibly due to the L and F contributions in the M ratio, whose activation energy by KAS and Starink was higher than that of the M sample. Generally, the average E_α of all the DPWP from the FWO model was lower than that reported for common biomasses such as rice husks ($221.2 \pm 22.3 \text{ kJ mol}^{-1}$) and elephant grass ($218.1 \pm 26.4 \text{ kJ mol}^{-1}$) [60]. Moreover, the E_α of M ($57.1 \pm 25.6 \text{ kJ mol}^{-1}$) by FWO was closely similar to that of red algae (57.0 kJ mol^{-1}) [66]. We presumed that the difference in the E_α was plausibly due to the variation in biomass type, growth conditions, and the biomass composition [36]. Activation energy can be through molecular transition theory, where only molecules with enough kinetic energy can overcome a reaction energy barrier threshold to react and form products. Furthermore, activation energy can be due to transition state theory, which is the difference between the average energy of molecules under reaction conditions and the average energy of all participating reactant molecules [67]. This implies that samples with low activation energy would easily be pyrolyzable. On this basis and as representative of all other parts, the M sample was the most suitable sample for the pyrolysis of date palm waste into bio-products.

Leaflet (L), rachis (R), fibers (F), composite (M), and the enthalpy, ΔH is a thermodynamic property of state function arising from heat absorbed or released during a chemical reaction, often involving chemical bond dissociation under constant pressure. Furthermore, Figure 4 shows the plot of enthalpy change against the conversion rate of DPWP as determined by the FWO, KAS, and Starink methods. All enthalpies calculated by FWO had similar values for all samples at all conversion conditions, except at very high temperature (i.e., $E_\alpha = 0.9$), where F and L ΔH was noticeably higher than that of R and M samples. From KAS models, the L and F had close ΔH values until up to $E_\alpha = 0.7$ and beyond this point, the ΔH values of F were higher than that of L. The R samples had the least ΔH followed by M. Similar ΔH trend from KAS was observed in the Starink model except that the R evinced ΔH higher than that of M.

Table 4. The average activation energies and thermodynamic parameters of leaflet (L), rachis (R), fiber (F), and (d) composite (M) samples of DPWP determined by three model-free methods.

| DPWP | FWO | | | | KAS | | | | Starink | | | |
|------|---------------------------------|--------------------------------|-------------------------------|------------------------------|---------------------------------|--------------------------------|-------------------------------|------------------------------|---------------------------------|--------------------------------|-------------------------------|------------------------------|
| | $E_{\alpha}/\text{kJ mol}^{-1}$ | $\text{Log A (s}^{-1}\text{)}$ | $\Delta G/\text{kJ mol}^{-1}$ | $\Delta S/\text{J mol}^{-1}$ | $E_{\alpha}/\text{kJ mol}^{-1}$ | $\text{Log A (s}^{-1}\text{)}$ | $\Delta G/\text{kJ mol}^{-1}$ | $\Delta S/\text{J mol}^{-1}$ | $E_{\alpha}/\text{kJ mol}^{-1}$ | $\text{Log A (s}^{-1}\text{)}$ | $\Delta G/\text{kJ mol}^{-1}$ | $\Delta S/\text{J mol}^{-1}$ |
| L | 163.97 ± 40.1 | 13.66 ± 1.2 | 193.77 ± 40.1 | −0.068 ± 0.02 | 667.52 ± 225.8 | 56.36 ± 8.1 | 186.51 ± 38.2 | 0.742 ± 0.13 | 647.29 ± 218.7 | 54.64 ± 7.8 | 186.67 ± 38.4 | 0.710 ± 0.13 |
| R | 157.97 ± 25.7 | 26.75 ± 1.9 | 93.19 ± 20.9 | 0.201 ± 0.04 | 463.46 ± 114.3 | 76.43 ± 2.1 | 90.33 ± 28.8 | 1.152 ± 0.04 | 451.08 ± 110.6 | 74.42 ± 1.9 | 90.40 ± 28.8 | 1.114 ± 0.04 |
| F | 169.14 ± 51.8 | 26.91 ± 2.6 | 107.09 ± 45.1 | 0.183 ± 0.06 | 684.61 ± 261.2 | 107.08 ± 3.6 | 99.29 ± 34.9 | 1.625 ± 0.1 | 663.92 ± 2253.7 | 103.86 ± 3.5 | 99.38 ± 34.9 | 1.568 ± 0.09 |
| M | 157.04 ± 25.6 | 13.82 ± 1.0 | 184.30 ± 28.6 | −0.054 ± 0.02 | 466.78 ± 115.4 | 41.31 ± 4.9 | 178.91 ± 27.3 | 0.467 ± 0.08 | 454.22 ± 128.6 | 29.54 ± 6.9 | 180.58 ± 27.0 | 0.242 ± 0.12 |

In addition, the relationship between E_α and ΔH was investigated as shown in Figure 5. Little or no difference between E_α and ΔH was observed. This closeness indicates the formation of the activation complex and insignificant additional energy that might be required to form the product [68]. For instance, petroleum fuels (such paraffin and naphtha) have a broad range of carbon number distributions with varying bond energies that might require higher energy at a wide temperature range to break the intramolecular bonds [69]. Similarly, DPWP consists of fractions of hemicellulose, cellulose, and lignin (lignocellulosic-based complex) with varying carbon number distributions. Therefore, thermal decomposition of such a complex might involve varying bond dissociation energies at a wide temperature profile, as we have observed. Moreover, all the samples' ΔH values were positive, which signifies an endothermic pyrolysis reaction [70]. The L and M samples in Table 4 and Tables S1–S4 for the FWO model showed negative entropy results. This means that the degree of disorder for products was less than that of the reactants due to bond dissociations [37]. This also confirmed that the bond dissociation of the reactants was attributed to the heat input into the system. Based on reaction energy, the M sample required lower activation energy and enthalpy than other investigated DPWP. By comparison, the average ΔG values of the rachis sample (R) were much lower by almost twice the highest values of the leaflet samples (L) across all models. In addition, the ΔG values of R were three times lower at lower conversions and almost twice as high as those of L at the same conversion conditions. Based on the first and second laws of thermodynamics, the big ΔG values and small ΔS suggests that the driving force between the L and M samples was a non-spontaneous reaction. The range of the average ΔG values of DPWP for all models (90.33–193.77 kJ/mol) were similar to those reported with rice straw (164.594–180.143 kJ/mol), dairy product (165.086–176.6 kJ/mol), and chicken manure (158.906–175.299 kJ/mol) [71]. The Gibb's free energy gives more information on how favored a reaction is to reach chemical equilibrium [72].

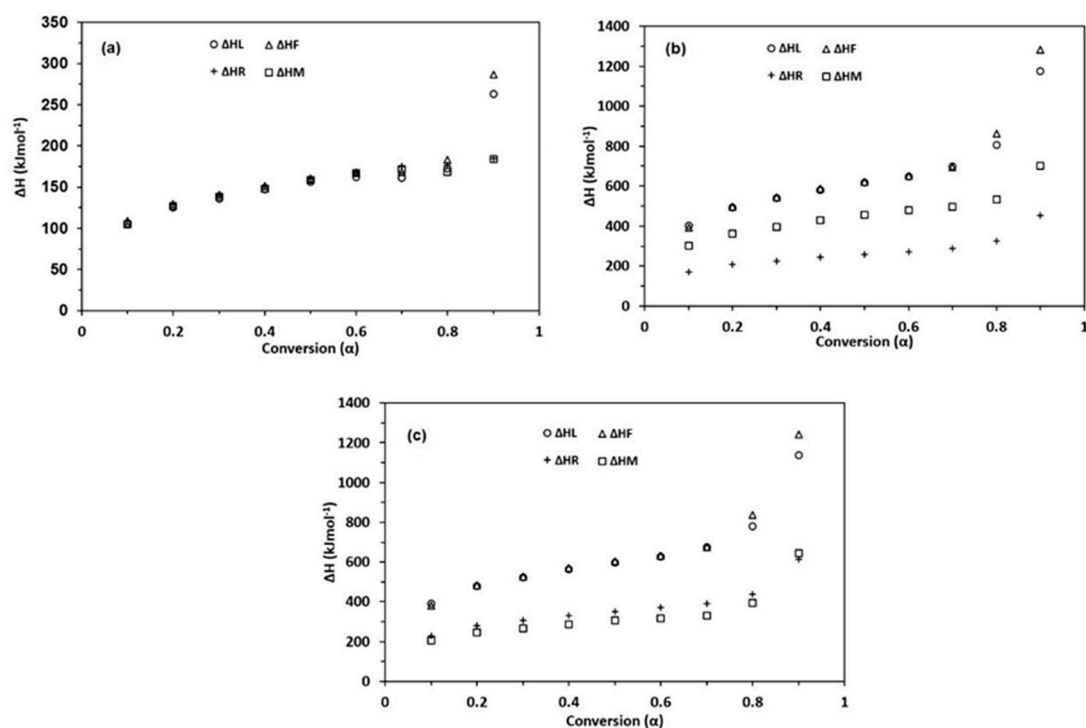


Figure 4. The enthalpy changes of DPWP as determined by the (a) FWO, (b) KAS, and (c) Starink model-free methods.

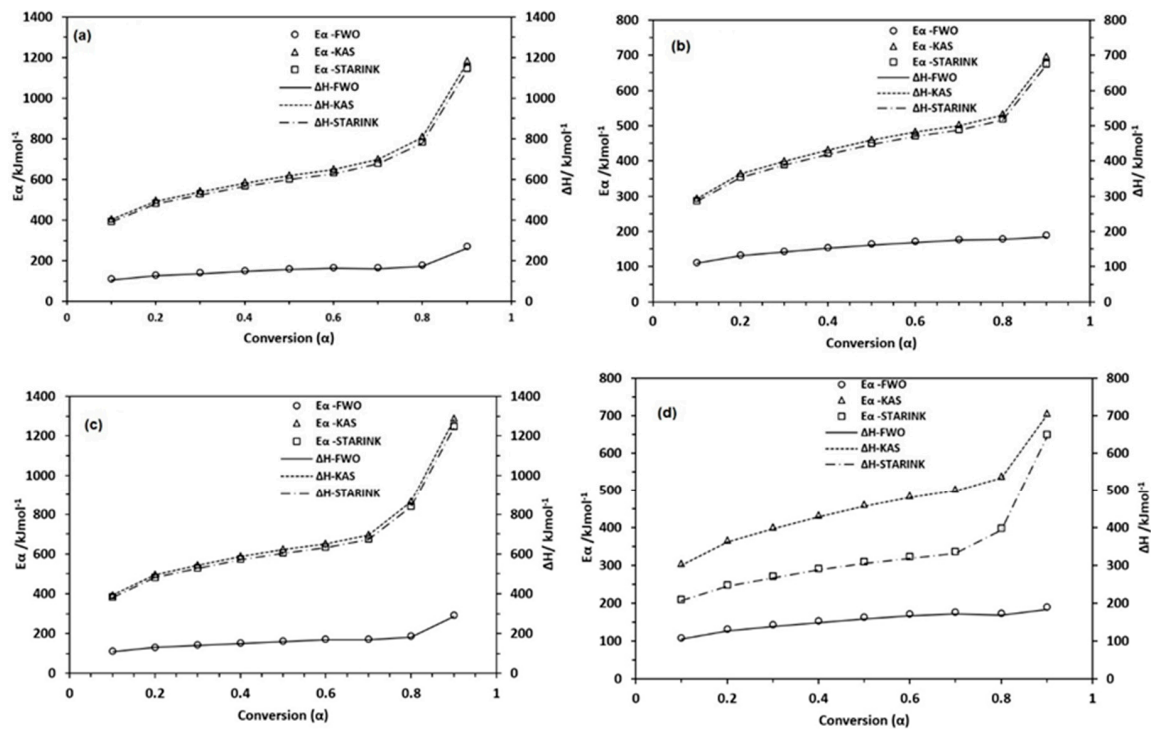


Figure 5. Combined activation energies and enthalpies of DPWP for (a) leaflet (L), (b) rachis (R), (c) fibers (F), and (d) composite (M) by three model-free methods.

3.6. Reaction Model Determination

3.6.1. Malek Method

The Malek method, expressed by Equation (1), is used to determine the probable reaction mechanism involving heterogeneous reaction [73].

$$Z(\alpha) = f(\alpha)g(\alpha) = \left(\frac{d\alpha}{dt}\right)_{\alpha} T_{\alpha}^2 \left[\frac{\Pi(x)}{\beta T_{\alpha}}\right] \quad (1)$$

where, $\left(\frac{d\alpha}{dt}\right)_{\alpha}$ is rate of reaction at a given conversion, α , and heating rate, β , $\Pi(x)$ approximates temperature integral profile and $x = E_{\alpha}/RT_{\alpha}$. The x values used were in a range of 5–20 and the temperature approximation $\Pi(x)$ function is defined by Equation (2) [74].

$$(x) = \frac{x^3 + 18x^3 + 88x + 96}{x^4 + 20x^3 + 120x^3 + 240x + 120} \quad (2)$$

The theoretical $z(\alpha)$ plots against α depend on $f(\alpha)$ and $g(\alpha)$ functions, whereas the experimental $z(\alpha)$ values are determined for a specific value $\frac{d\alpha}{dt}$, E_{α} and T_{α} using a known heating rate. The known theoretical model functions give the basis of comparison with the experimental $z(\alpha)$ master plots [34,57,75]. The best fit between the experimental and theoretical models gives the probable biomass reaction mechanism.

Figures S4–S7 show the results of the experimental $z(\alpha)$ master plots and fitted model plots of DPWP biomass waste, obtained using model-free methods.

The experimental and the fitted $z(\alpha)$ master plots showed a similar trend in all samples for all three model-free methods at all the studied heating rates. The correlation coefficient was between 0.8913 and 0.9664, which means that the model described the data with 89.13 and 96.64% accuracy. The best-fitting trend followed the order of $F > L > M > R$ at heating rates of 20, 20, 25, and 25 °C min⁻¹, respectively. The data were fit with polynomial curves of $n = 4$, implying a fourth order dimension Avrami–Erofeev

model. This type of model is characterized by multidimensional nuclei and the random growth reaction mechanism with a polynomial equation as $(g(\alpha) = [-\ln(1 - \alpha)]^{\frac{1}{n}})$ [76]. These random growths and nucleation caused thermodynamic inhibition, leading to differing activation energies arising from processes such as hydration and imperfections of the sample crystallite particle size [77].

3.6.2. Popescu Method

This is another common integral method that can be used to determine the mechanism of a reaction. This is based on varying heating rates for conversion α at the same temperature and is defined by Equation (3).

$$G(\alpha)_{mn} = \int_{\alpha_m}^{\alpha_n} \frac{d\alpha}{f(\alpha)} = \frac{1}{\beta} \int_{T_m}^{T_n} k(T) dT = \frac{1}{\beta} I(T)_{mn} \quad (3)$$

where α_n and α_m are conversion rates at corresponding temperatures T_n and T_m , respectively, whereas $k(T)$ is the reaction rate constant [76]. The method is dependent on the choice of T_n and T_m , and in an experiment, the $(I(T)_{mn})$ value is constant, irrespective of the temperature. Unlike the Malek method that requires approximation of the temperature integral, the main advantage of the Popescu method is that prior activation energy determination and assumption on temperature integral are not required, thus, it exhibits superior accuracy in model prediction. However, the technique has a shortcoming: in the case of a poor choice of T_n and T_m , it could lead to erroneous results. To minimize such errors, a wide temperature range of T_n, T_m , between 170 °C and 700 °C was considered to determine the $G(\alpha)_{mn}$ values at different heating rates. The ignition and burnout temperatures are often reported as good guiding tools for the choice of T_n and T_m [78]. Due to the lack of instruments to determine the T_n and T_m chosen were assumed to fall in the range of the DPWP ignition and burnout temperatures.

To determine the reaction mechanism, a linear plot of $G(\alpha)_{mn}$ versus $\frac{1}{\beta}$ with an intercept $(I(T)_{mn})$ passing through zero was made [79]. The plot with an intercept close or equal to zero and R^2 close or equal to 1 describes the best possible reaction mechanism. Table S5 shows the linear fitting mechanism functions by the Popescu method for different parts of date palm waste biomass. The FWO model-free method showed better $I(T)_{mn}$ results, with the trend as $M > R > F > L$. Furthermore, the KAS and Starink models for all samples evinced excellent plots with reliable correlation coefficients, R^2 . Additionally, the $G(\alpha)_{mn}$ versus $\frac{1}{\beta}$ straight lines were dependent on the random nucleation and nuclei growth mechanism as defined by the Avrami–Erofeev equation [80]. Therefore, the linear plot results of the Popescu method suggest that all DPWP biomass follows the random nucleation and nuclei growth mechanism defined by Avrami–Erofeev $(g(\alpha) = [-\ln(1 - \alpha)]^{\frac{1}{4}})$.

3.6.3. Evaluation of the Reaction Model $g(\alpha)$

Finally, the compensation effect parameters were obtained by reconstructing the model numerically with the predetermined $E\alpha$ and $A(\alpha)$ from the model-free methods. Figure S8 showed a good linear fitting of the experimental results to the equation of kinetic compensation effects $(\ln A = aE + b)$. We observed a high correlation coefficient of 0.95–0.99. This strong relationship between activation energy and pre-exponential factor signifies the existence of kinetic compensation effects for the combustion of L, R, F, and M, which is consistent with that suggested by the Avrami kinetic model [56]. Furthermore, the model was reconstructed using Equations (13) and (14) in a reference article [81]. Figure S9 shows the $g(\alpha)/g(0.5)$ remodeled from the experimental data and the chosen Avrami mechanism function ($n = 4$). The experimental n values ranged between 4 and 5, with an average value of 4.25 ± 0.45 and an average correlation coefficient of 0.9917 ± 0.01 , for all investigated DPWP. There was an overlap between the experimental data and the theoretical model curve. Similar results were reported for the pyrolysis of reed canary [81].

4. Conclusions

Non-isothermal kinetic and thermodynamic behaviors of different DPWP were studied at different heating rates using model-free methods, and the following conclusions were drawn. All DPWP showed good energy potential with high average total volatile matter and high heating value. The DPWP TGA results revealed the main mass loss at Stage-II with the average mass loss trend of $R > M > L > F$ at 127–398 °C. The lowest and highest activation energies were quantitated by the FWO model for M and F, respectively. There was an observed strong relationship between the activation energy and enthalpy, and the overall pyrolysis was endothermic. Regarding the chemical equilibrium, the KAS model performed best, indicating the ΔG value trend of $R > F > M > L$. The reaction mechanism of all DPWP was described by the Avrami–Erofeev model mechanism, characterized by random and multidimensional nuclei growth. Additionally, kinetic compensation effects were observed for all pyrolytic processes. Consequently, the high volatile matter, energy content, low energy barriers across a wide range of temperature, and thermodynamic feasibility associated with the pyrolysis of DPWP profess it as a viable energy-biomass candidate in the biorefinery. However, further examination on how the proposed reaction mechanism happens is required. Future works may include pyrolysis of the same waste parts in a tube furnace as a step forward to implementation in a biorefinery. Furthermore, the results of this study will be used during the thermal chemical conversion of DPWP to high value chemical precursors.

Supplementary Materials: The following are available online at <http://www.mdpi.com/1996-1073/13/24/6553/s1> Tables S1–S5 and Figures S1–S9 demonstrate the data that support the analysis and discussion in Sections 3.5 and 3.6 (kinetic, thermodynamic parameters and reaction mechanism).

Author Contributions: Conceptualization, E.G. and A.H.A.-M.; Methodology, E.G.; Formal analysis and investigation, A.H.A.-M., A.A.K., and M.M.A.-O.; Resources, A.H.A.-M. and A.A.K.; Writing—original draft preparation, E.G.; Writing—review and editing, A.H.A.-M., A.A.K., and M.M.A.-O.; Supervision, A.H.A.-M., A.A.K., and M.M.A.-O.; Project administration, A.H.A.-M.; Funding acquisition, A.H.A.-M. and M.M.A.-O. All authors have read and agreed to the published version of the manuscript.

Funding: This research received no external funding.

Acknowledgments: This research was funded by the UAEU Emirates Center for Energy and Environment (31R107).

Conflicts of Interest: The authors declare no conflict of interest.

References

1. Lewis, N.S.; Crabtree, G.; Nozik, A.J.; Wasielewski, M.R.; Alivisatos, P.; Kung, H.; Tsao, J.; Chandler, E.; Walukiewicz, W.; Spitler, M. *Basic Research Needs for Solar Energy Utilization. Report of the Basic Energy Sciences Workshop on Solar Energy Utilization, April 18–21, 2005*; DOESC (USDOE Office of Science (SC)), USA: Washington, DC, USA, 2005.
2. Energy, G. *CO2 Status Report—The Latest Trends in Energy and Emissions in 2018*; International Energy Agency: Paris, France, 2019.
3. Razzaq, L.; Farooq, M.; Mujtaba, M.A.; Sher, F.; Farhan, M.; Hassan, M.T.; Soudagar, M.E.M.; Atabani, A.E.; Kalam, M.A.; Imran, M. Modeling viscosity and density of ethanol-diesel-biodiesel ternary blends for sustainable environment. *Sustainability* **2020**, *12*, 5186. [[CrossRef](#)]
4. Al-Juboori, O.; Sher, F.; Khalid, U.; Niazi, M.B.K.; Chen, G.Z. Electrochemical production of sustainable hydrocarbon fuels from CO2 co-electrolysis in eutectic molten melts. *ACS Sustain. Chem. Eng.* **2020**, *8*, 12877–12890. [[CrossRef](#)]
5. Zhang, Y.; Fang, Y.; Jin, B.; Zhang, Y.; Zhou, C.; Sher, F. Effect of slot wall jet on combustion process in a 660 MW opposed wall fired pulverized coal boiler. *Int. J. Chem. React. Eng.* **2019**, *17*, 1–13. [[CrossRef](#)]
6. Agency, E.P. Emission Control Technologies. Available online: https://www.epa.gov/sites/production/files/2015-07/documents/chapter_5_emission_control_technologies.pdf (accessed on 18 November 2020).
7. Cheremisinoff, N.P.; Rosenfeld, P. *Handbook of Pollution Prevention and Cleaner Production Volume 3: Best Practices in the Agrochemical Industry*; William Andrew: Norwich, NY, USA, 2010; Volume 3.

8. Zhang, T.; Yang, Y.; Ni, J.; Xie, D. Adoption behavior of cleaner production techniques to control agricultural non-point source pollution: A case study in the Three Gorges Reservoir Area. *J. Clean. Prod.* **2019**, *223*, 897–906. [[CrossRef](#)]
9. Tillman, D.A. *Fuels and Energy from Renewable Resources*; Elsevier: Amsterdam, The Netherlands, 2012.
10. Hassan, M.H.A.; Sher, F.; Zarren, G.; Suleiman, N.; Tahir, A.A.; Snape, C.E. Kinetic and thermodynamic evaluation of effective combined promoters for CO₂ hydrate formation. *J. Nat. Gas Sci. Eng.* **2020**, *78*, 103313. [[CrossRef](#)]
11. Duncan, M. *Biomass Energy—Optimising Its Contribution to Poverty Reduction and Ecosystem Services*; International Institute for Environment and Development: London, UK, 2011; pp. 1–93.
12. Sher, F.; Yaqoob, A.; Saeed, F.; Zhang, S.; Jahan, Z.; Klemeš, J.J. Torrefied biomass fuels as a renewable alternative to coal in co-firing for power generation. *Energy* **2020**, *209*, 118444. [[CrossRef](#)]
13. Cheali, P.; Posada, J.A.; Gernaey, K.V.; Sin, G. Economic risk analysis and critical comparison of optimal biorefinery concepts. *BiofuelsBioprod. Biorefin.* **2016**, *10*, 435–445. [[CrossRef](#)]
14. Rødsrud, G.; Lersch, M.; Sjöde, A. History and future of world's most advanced biorefinery in operation. *Biomass Bioenergy* **2012**, *46*, 46–59. [[CrossRef](#)]
15. Cheali, P.; Quaglia, A.; Gernaey, K.V.; Sin, G. Effect of Market Price Uncertainties on the Design of Optimal Biorefinery Systems A Systematic Approach. *Ind. Eng. Chem. Res.* **2014**, *53*, 6021–6032. [[CrossRef](#)]
16. Bozell, J.J. An evolution from pretreatment to fractionation will enable successful development of the integrated biorefinery. *BioResources* **2010**, *5*, 1326–1327.
17. Beer, C.; Reichstein, M.; Tomelleri, E.; Ciais, P.; Jung, M.; Carvalhais, N.; Rödenbeck, C.; Arain, M.A.; Baldocchi, D.; Bonan, G.B. Terrestrial gross carbon dioxide uptake: Global distribution and covariation with climate. *Science* **2010**, *329*, 834–838. [[CrossRef](#)] [[PubMed](#)]
18. Liao, J.C.; Mi, L.; Pontrelli, S.; Luo, S. Fuelling the future: Microbial engineering for the production of sustainable biofuels. *Nat. Rev. Microbiol.* **2016**, *14*, 288. [[CrossRef](#)] [[PubMed](#)]
19. Vakkilainen, E.; Kuparinen, K.; Heinimö, J. *Large Industrial Users of Energy Biomass*; IEA: Paris, France, 2013; p. 2013.
20. Taheripour, F.; Tyner, W.E. Welfare assessment of the renewable fuel standard: Economic efficiency, rebound effect, and policy interactions in a general equilibrium framework. In *Modeling, Dynamics, Optimization and Bioeconomics I*; Springer: New York, NY, USA, 2014; pp. 613–632.
21. Rahdar, M.; Wang, L.; Hu, G. Potential competition for biomass between biopower and biofuel under RPS and RFS2. *Appl. Energy* **2014**, *119*, 10–20. [[CrossRef](#)]
22. Berndes, G.; Hoogwijk, M.; Van den Broek, R. The contribution of biomass in the future global energy supply: A review of 17 studies. *Biomass Bioenergy* **2003**, *25*, 1–28. [[CrossRef](#)]
23. Müller-Hagedorn, M.; Bockhorn, H.; Krebs, L.; Müller, U. A comparative kinetic study on the pyrolysis of three different wood species. *J. Anal. Appl. Pyrolysis* **2003**, *68*, 231–249. [[CrossRef](#)]
24. Winchester, N.; Reilly, J.M. The feasibility, costs, and environmental implications of large-scale biomass energy. *Energy Econ.* **2015**, *51*, 188–203. [[CrossRef](#)]
25. Bridgwater, A.V. Review of fast pyrolysis of biomass and product upgrading. *Biomass Bioenergy* **2012**, *38*, 68–94. [[CrossRef](#)]
26. Mohan, D.; Pittman, C.U., Jr.; Steele, P.H. Pyrolysis of wood/biomass for bio-oil: A critical review. *Energy Fuels* **2006**, *20*, 848–889. [[CrossRef](#)]
27. Shang, G.; Li, Q.; Liu, L.; Chen, P.; Huang, X. Adsorption of hydrogen sulfide by biochars derived from pyrolysis of different agricultural/forestry wastes. *J. Air Waste Manag. Assoc.* **2016**, *66*, 8–16. [[CrossRef](#)]
28. Papurello, D.; Boschetti, A.; Silvestri, S.; Khomenko, I.; Biasioli, F. Real-time monitoring of removal of trace compounds with PTR-MS: Biochar experimental investigation. *Renew. Energy* **2018**, *125*, 344–355. [[CrossRef](#)]
29. Zhu, H.L.; Papurello, D.; Gandiglio, M.; Lanzini, A.; Akpınar, I.; Shearing, P.R.; Manos, G.; Brett, D.J.L.; Zhang, Y.S. Study of H₂S removal capability from simulated biogas by using waste-derived adsorbent materials. *Processes* **2020**, *8*, 1030. [[CrossRef](#)]
30. Ibbett, R.; Gaddipati, S.; Davies, S.; Hill, S.; Tucker, G. The mechanisms of hydrothermal deconstruction of lignocellulose: New insights from thermal-analytical and complementary studies. *Bioresour. Technol.* **2011**, *102*, 9272–9278. [[CrossRef](#)] [[PubMed](#)]
31. Mabuda, A.I.; Mamphweli, N.S.; Meyer, E.L. Model free kinetic analysis of biomass/sorbent blends for gasification purposes. *Renew. Sustain. Energy Rev.* **2016**, *53*, 1656–1664. [[CrossRef](#)]

32. Graham, R.G.; Bergougnou, M.A.; Overend, R.P. Fast pyrolysis of biomass. *J. Anal. Appl. Pyrolysis* **1984**, *6*, 95–135. [\[CrossRef\]](#)
33. Slopiecka, K.; Bartocci, P.; Fantozzi, F. Thermogravimetric analysis and kinetic study of poplar wood pyrolysis. *Appl. Energy* **2012**, *97*, 491–497. [\[CrossRef\]](#)
34. White, J.E.; Catallo, W.J.; Legendre, B.L. Biomass pyrolysis kinetics: A comparative critical review with relevant agricultural residue case studies. *J. Anal. Appl. Pyrolysis* **2011**, *91*, 1–33. [\[CrossRef\]](#)
35. Wu, W.; Cai, J.; Liu, R. Isoconversional kinetic analysis of distributed activation energy model processes for pyrolysis of solid fuels. *Ind. Eng. Chem. Res.* **2013**, *52*, 14376–14383. [\[CrossRef\]](#)
36. Huang, L.; Ding, T.; Liu, R.; Cai, J. Prediction of concentration profiles and theoretical yields in lignocellulosic biomass pyrolysis. *J. Therm. Anal. Calorim.* **2015**, *120*, 1473–1482. [\[CrossRef\]](#)
37. Kim, Y.S.; Kim, Y.S.; Kim, S.H. Investigation of thermodynamic parameters in the thermal decomposition of plastic waste– waste lube oil compounds. *Environ. Sci. Technol.* **2010**, *44*, 5313–5317. [\[CrossRef\]](#)
38. Mukherjee, A.; Das, P.; Minu, K. Thermogravimetric analysis and kinetic modelling studies of selected agro-residues and biodiesel industry wastes for pyrolytic conversion to bio-oil. *Biomass Convers. Biorefinery* **2014**, *4*, 259–268. [\[CrossRef\]](#)
39. Cai, J.; Xu, D.; Dong, Z.; Yu, X.; Yang, Y.; Banks, S.W.; Bridgwater, A.V. Processing thermogravimetric analysis data for isoconversional kinetic analysis of lignocellulosic biomass pyrolysis: Case study of corn stalk. *Renew. Sustain. Energy Rev.* **2018**, *82*, 2705–2715. [\[CrossRef\]](#)
40. Jiang, G.; Wei, L. Analysis of Pyrolysis Kinetic Model for Processing of Thermogravimetric Analysis Data. *Phase Chang. Mater. Appl.* **2018**, *143*. [\[CrossRef\]](#)
41. Dong, Z.; Yang, Y.; Cai, W.; He, Y.; Chai, M.; Liu, B.; Yu, X.; Banks, S.W.; Zhang, X.; Bridgwater, A.V. Theoretical analysis of double Logistic distributed activation energy model for thermal decomposition kinetics of solid fuels. *Ind. Eng. Chem. Res.* **2018**, *57*, 7817–7825. [\[CrossRef\]](#)
42. Khawam, A. Application of Solid-State Kinetics to Desolvation Reactions. Ph.D. Thesis, University of Iowa, Iowa, IA, USA, 2007.
43. Heydari, M.; Rahman, M.; Gupta, R. Kinetic study and thermal decomposition behavior of lignite coal. *Int. J. Chem. Eng.* **2015**, *2015*, 9–10. [\[CrossRef\]](#)
44. Sait, H.H.; Hussain, A.; Salema, A.A.; Ani, F.N. Pyrolysis and combustion kinetics of date palm biomass using thermogravimetric analysis. *Bioresour. Technol.* **2012**, *118*, 382–389. [\[CrossRef\]](#)
45. Makkawi, Y.; El Sayed, Y.; Salih, M.; Nancarrow, P.; Banks, S.; Bridgwater, T. Fast pyrolysis of date palm (*Phoenix dactylifera*) waste in a bubbling fluidized bed reactor. *Renew. Energy* **2019**, *143*, 719–730. [\[CrossRef\]](#)
46. Bensidhom, G.; Hassen-Trabelsi, A.B.; Alper, K.; Sghairoun, M.; Zaafour, K.; Trabelsi, I. Pyrolysis of date palm waste in a fixed-bed reactor: Characterization of pyrolytic products. *Bioresour. Technol.* **2018**, *247*, 363–369. [\[CrossRef\]](#)
47. Galiwango, E.; Rahman, N.S.A.; Al-Marzouqi, A.H.; Abu-Omar, M.M.; Khaleel, A.A. Isolation and characterization of cellulose and α -cellulose from date palm biomass waste. *Heliyon* **2019**, *5*, e02937. [\[CrossRef\]](#)
48. Yokoyama, S.; Matsumura, Y. The Asian biomass handbook: A guide for biomass production and utilization. *Jpn. Inst. Energy* **2008**, 61–62.
49. Obernberger, I.; Biedermann, F.; Widmann, W.; Riedl, R. Concentrations of inorganic elements in biomass fuels and recovery in the different ash fractions. *Biomass Bioenergy* **1997**, *12*, 211–224. [\[CrossRef\]](#)
50. Sluiter, A.; Hames, B.; Ruiz, R.; Scarlata, C.; Sluiter, J.; Templeton, D.; Crocker, D. Determination of structural carbohydrates and lignin in biomass. *Lab. Anal. Proced.* **2008**, *1617*, 1–16.
51. Dence, C.W. The determination of lignin. In *Methods in Lignin Chemistry*; Springer: New York, NY, USA, 1992; pp. 33–61.
52. Sotoudehnia, F.; Rabiou, A.B.; Alayat, A.; McDonald, A.G. Characterization of bio-oil and biochar from pyrolysis of waste corrugated cardboard. *J. Anal. Appl. Pyrolysis* **2020**, *145*, 104722. [\[CrossRef\]](#)
53. Suman, S.; Panwar, D.S.; Gautam, S. Surface morphology properties of biochars obtained from different biomass waste. *Energy Sources Part A Recovery Util. Environ. Eff.* **2017**, *39*, 1007–1012. [\[CrossRef\]](#)
54. Sher, F.; Iqbal, S.Z.; Albazzaz, S.; Ali, U.; Mortari, D.A.; Rashid, T. Development of biomass derived highly porous fast adsorbents for post-combustion CO₂ capture. *Fuel* **2020**, *282*, 118506. [\[CrossRef\]](#)

55. Jubeen, F.; Liaqat, A.; Amjad, F.; Sultan, M.; Iqbal, S.Z.; Sajid, I.; Khan Niazi, M.B.; Sher, F. Synthesis of 5-Fluorouracil Cocrystals with Novel Organic Acids as Coformers and Anticancer Evaluation against HCT-116 Colorectal Cell Lines. *Cryst. Growth Des.* **2020**, *20*, 2406–2414. [[CrossRef](#)]
56. Hu, Y.; Wang, Z.; Cheng, X.; Ma, C. Non-isothermal TGA study on the combustion reaction kinetics and mechanism of low-rank coal char. *RSC Adv.* **2018**, *8*, 22909–22916. [[CrossRef](#)]
57. Shuping, Z.; Yulong, W.; Mingde, Y.; Chun, L.; Junmao, T. Pyrolysis characteristics and kinetics of the marine microalgae *Dunaliella tertiolecta* using thermogravimetric analyzer. *Bioresour. Technol.* **2010**, *101*, 359–365. [[CrossRef](#)]
58. Wang, C.; Zhao, B.; Tian, X.; Wang, K.; Tian, Z.; Han, W.; Bian, H. Study on the Pyrolysis Kinetics and Mechanisms of the Tread Compounds of Silica-Filled Discarded Car Tires. *Polymers* **2020**, *12*, 810. [[CrossRef](#)]
59. Jeguirim, M.; Dorge, S.; Trouvé, G. Thermogravimetric analysis and emission characteristics of two energy crops in air atmosphere: *Arundo donax* and *Miscanthus giganteus*. *Bioresour. Technol.* **2010**, *101*, 788–793. [[CrossRef](#)]
60. Braga, R.M.; Melo, D.M.A.; Aquino, F.M.; Freitas, J.C.O.; Melo, M.A.F.; Barros, J.M.F.; Fontes, M.S.B. Characterization and comparative study of pyrolysis kinetics of the rice husk and the elephant grass. *J. Therm. Anal. Calorim.* **2014**, *115*, 1915–1920. [[CrossRef](#)]
61. Biney, P.O.; Gyamerah, M.; Shen, J.; Menezes, B. Kinetics of the pyrolysis of arundo, sawdust, corn stover and switch grass biomass by thermogravimetric analysis using a multi-stage model. *Bioresour. Technol.* **2015**, *179*, 113–122. [[CrossRef](#)] [[PubMed](#)]
62. Mohammed, M.A.A.; Salmiaton, A.; Azlina, W.W.; Amran, M.S.M. Gasification of oil palm empty fruit bunches: A characterization and kinetic study. *Bioresour. Technol.* **2012**, *110*, 628–636. [[CrossRef](#)] [[PubMed](#)]
63. Lapuerta, M.; Hernández, J.J.; Rodríguez, J. Kinetics of devolatilisation of forestry wastes from thermogravimetric analysis. *Biomass Bioenergy* **2004**, *27*, 385–391. [[CrossRef](#)]
64. Lin, B.; Zhou, J.; Qin, Q.; Song, X.; Luo, Z. Thermal behavior and gas evolution characteristics during co-pyrolysis of lignocellulosic biomass and coal: A TG-FTIR investigation. *J. Anal. Appl. Pyrolysis* **2019**, *144*, 104718. [[CrossRef](#)]
65. Carrier, M.; Auret, L.; Bridgwater, A.; Knoetze, J.H. Using apparent activation energy as a reactivity criterion for biomass pyrolysis. *Energy Fuels* **2016**, *30*, 7834–7841. [[CrossRef](#)]
66. Li, D.; Chen, L.; Zhang, X.; Ye, N.; Xing, F. Pyrolytic characteristics and kinetic studies of three kinds of red algae. *Biomass Bioenergy* **2011**, *35*, 1765–1772. [[CrossRef](#)]
67. Galwey, A.K.; Brown, M.E. Application of the Arrhenius equation to solid state kinetics: Can this be justified? *Thermochim. Acta* **2002**, *386*, 91–98. [[CrossRef](#)]
68. Vlaev, L.T.; Georgieva, V.G.; Genieva, S.D. Products and kinetics of non-isothermal decomposition of vanadium (IV) oxide compounds. *J. Therm. Anal. Calorim.* **2007**, *88*, 805–812. [[CrossRef](#)]
69. Savage, P.E. Mechanisms and kinetics models for hydrocarbon pyrolysis. *J. Anal. Appl. Pyrolysis* **2000**, *54*, 109–126. [[CrossRef](#)]
70. Daugaard, D.E.; Brown, R.C. Enthalpy for pyrolysis for several types of biomass. *Energy Fuels* **2003**, *17*, 934–939. [[CrossRef](#)]
71. Xu, Y.; Chen, B. Investigation of thermodynamic parameters in the pyrolysis conversion of biomass and manure to biochars using thermogravimetric analysis. *Bioresour. Technol.* **2013**, *146*, 485–493. [[CrossRef](#)] [[PubMed](#)]
72. Coker, A.K. *Ludwig's Applied Process Design for Chemical and Petrochemical Plants*; Gulf Professional Publishing: Houston, TX, USA, 2014.
73. Málek, J. The kinetic analysis of non-isothermal data. *Thermochim. Acta* **1992**, *200*, 257–269. [[CrossRef](#)]
74. Senum, G.I.; Yang, R. Rational approximations of the integral of the Arrhenius function. *J. Therm. Anal. Calorim.* **1977**, *11*, 445–447. [[CrossRef](#)]
75. Stanko, M.; Stommel, M. Kinetic prediction of fast curing polyurethane resins by model-free isoconversional methods. *Polymers* **2018**, *10*, 698. [[CrossRef](#)]
76. El-Oyoun, M.A. An investigation of the kinetic transformation mechanism of Ge₁₂ 5Te₈₇ 5 chalcogenide glass under non-isothermal regime. *J. Non-Cryst. Solids* **2011**, *357*, 1729–1735. [[CrossRef](#)]
77. Burnham, A.K.; Weese, R.K.; Weeks, B.L. A distributed activation energy model of thermodynamically inhibited nucleation and growth reactions and its application to the β - δ phase transition of HMX. *J. Phys. Chem. B* **2004**, *108*, 19432–19441. [[CrossRef](#)]

78. Shamsipur, M.; Pourmortazavi, S.M.; Hajimirsadeghi, S.S.; Atifeh, S.M. Effect of functional group on thermal stability of cellulose derivative energetic polymers. *Fuel* **2012**, *95*, 394–399. [[CrossRef](#)]
79. Popescu, C. Integral method to analyze the kinetics of heterogeneous reactions under non-isothermal conditions a variant on the Ozawa-Flynn-Wall method. *Thermochim. Acta* **1996**, *285*, 309–323. [[CrossRef](#)]
80. Sultana, U.K.; Gulshan, F.; Gafur, M.A.; Kurny, A.S.W. Kinetics of recovery of alumina from aluminium casting waste through fusion with sodium hydroxide. *Am. J. Mater. Eng. Technol.* **2013**, *1*, 30–34.
81. Alhumade, H.; da Silva, J.C.G.; Ahmad, M.S.; Çakman, G.; Yıldız, A.; Ceylan, S.; Elkamel, A. Investigation of pyrolysis kinetics and thermal behavior of Invasive Reed Canary (*Phalaris arundinacea*) for bioenergy potential. *J. Anal. Appl. Pyrolysis* **2019**, *140*, 385–392. [[CrossRef](#)]

Publisher's Note: MDPI stays neutral with regard to jurisdictional claims in published maps and institutional affiliations.



© 2020 by the authors. Licensee MDPI, Basel, Switzerland. This article is an open access article distributed under the terms and conditions of the Creative Commons Attribution (CC BY) license (<http://creativecommons.org/licenses/by/4.0/>).